

Provided for non-commercial research and education use.
Not for reproduction, distribution or commercial use.



This article appeared in a journal published by Elsevier. The attached copy is furnished to the author for internal non-commercial research and education use, including for instruction at the authors institution and sharing with colleagues.

Other uses, including reproduction and distribution, or selling or licensing copies, or posting to personal, institutional or third party websites are prohibited.

In most cases authors are permitted to post their version of the article (e.g. in Word or Tex form) to their personal website or institutional repository. Authors requiring further information regarding Elsevier's archiving and manuscript policies are encouraged to visit:

<http://www.elsevier.com/copyright>



Contents lists available at ScienceDirect

Thin Solid Films

journal homepage: www.elsevier.com/locate/tsf

The correlation between mechanical stress, thermal shift and refractive index in HfO_2 , Nb_2O_5 , Ta_2O_5 and SiO_2 layers and its relation to the layer porosity

O. Stenzel^{a,*}, S. Wilbrandt^a, N. Kaiser^a, M. Vinnichenko^b, F. Munnik^b, A. Kolitsch^b, A. Chuvilin^c, U. Kaiser^c, J. Ebert^d, S. Jakobs^e, A. Kaless^e, S. Wüthrich^f, O. Treichel^g, B. Wunderlich^h, M. Bitzer^h, M. Grösslⁱ

^a Fraunhofer IOF, Albert-Einstein-Str.7,07745 Jena, Germany

^b Forschungszentrum Dresden-Rossendorf, P.O. Box 510119, 01314 Dresden, Germany

^c Universität Ulm, 89069 Ulm, Germany

^d Laseroptik GmbH, Gneisenastraße 14, 30826, Germany

^e mso jena GmbH, Carl-Zeiss-Promenade 10, 07745 Jena, Germany

^f Evatec Ltd., Lochriet 1, 8890 Flums, Switzerland

^g S1 Optics GmbH, Lauterstr. 18, 72622 Nürtingen, Germany

^h Fresnel Optics GmbH, Flurstedter Marktweg 13, 99510 Apolda, Germany

ⁱ FISBA OPTIK AG, Rorschacher Strasse 268, 9016 St Gallen, Switzerland

ARTICLE INFO

Article history:

Received 20 November 2008

Received in revised form 30 April 2009

Accepted 7 May 2009

Available online 15 May 2009

Keywords:

Optical coatings

Optical properties

Stress

Structural properties

ABSTRACT

We present extended experimental material about optical and mechanical properties of oxide optical coating materials, deposited by electron beam evaporation, ion and plasma ion assisted evaporation, sputtering and ion plating. A clear correlation between these experimental data is established and understood as being caused by the different degree of the porosity of the films. This assumption has been verified by investigation of the layer structure and accompanying simulations of the effect of porosity on refractive index, layer stress and thermal shift. As a practical conclusion, we find that a certain pore fraction in the films is essential in order to get a valuable balance between optical and mechanical coating properties.

© 2009 Elsevier B.V. All rights reserved.

1. Introduction

It is well known, that the performance of optical coatings crucially depends on the production accuracy and reproducibility of *geometrical* coating parameters such as film thickness, surface smoothness, defect (pinhole) concentration and the like. On the other hand, excellent, environmentally stable and reproducible values of optical thin film *material* constants like refractive indices and small extinction coefficients are required as well. Ideally, the films should not have gradients of optical properties, and their refractive index and extinction coefficient should be independent of the film thickness. Therefore, formation of amorphous layers is favoured. Additional requirements on non-optical material properties like small mechanical stress are equally important [1–3].

From thin film theory it is well known, that for any spectral target defined at normal incidence and practically non-absorbing materials, the optimal design is achieved with a pair of materials that reveal a refractive index contrast as high as possible [4]. As a consequence of this general design recipe, there arises a need to optimize deposition techniques and conditions with the goal to maximize achievable

refractive indices of traditional high-index materials. In modern ion assisted versions of optical coating techniques, the high densification of the coating leads to film refractive indices close to or higher than reported bulk values [2]. Hereby the ion plating techniques and reactively pulsed magnetron sputtering are reported to deliver coatings with the highest refractive indices known today [5]. As an additional advantage of densification, the pore fraction is negligible, so that thermal shift contributions due to penetration of atmospheric water into pores are absent, hence the coatings exhibit thermally stable high refractive indices. The disadvantage is that the densification results in high compressive stress of the coatings, which may be disturbing in high end applications and therefore require special post-deposition treatments to relax the layer stress. Moreover, higher refractive indices are often accompanied with a somewhat higher extinction coefficient, so that the material with the highest index is not necessarily the best one with respect to the full complex of modern requirements.

Therefore, for a high-index coating material, a compromise between high refractive index, low extinction coefficient, small mechanical stress and negligible thermal shift is often required. But there is a lack of knowledge in how such a compromise would look like, and particularly, in how far a certain degree of porosity is required in the film to guarantee a good balance between the mentioned optical and mechanical properties.

* Corresponding author.

E-mail address: olaf.stenzel@iof.fraunhofer.de (O. Stenzel).

This study is aimed at understanding the relationship between thermal shift, refractive index and stress for three high-index coating materials (hafnium oxide, niobium pentoxide and tantalum pentoxide), deposited as single layers by different deposition techniques. For reference, the same investigations have been performed for silicon dioxide as a typical low-index material. The variety of deposition techniques enables the variation of the film morphology in a wide range and allows the correlation of the film's optical and mechanical properties to their porosity and hydrogen content of the samples.

This paper emphasizes the mutual correlation between optical and mechanical layer properties as well as their relation to the porosity of the coatings. It does not deal with the correlation between deposition parameters and achieved layer performance. The participating companies were even encouraged to prepare high quality coatings without the necessity to disclose their deposition parameters and recipes in detail.

2. Layer deposition

2.1. General philosophy

The layer deposition has been performed in terms of a round robin deposition experiment with participation of all authors of this study. Samples have been prepared and supplied by the companies mso jena, Laseroptik Garbsen, S1 Optics Nürtingen, Evatec Ltd. Flums, Fresnel Optics Apolda and FISBA OPTIK St. Gallen. Additional samples have been prepared by the participating research institutes Fraunhofer IOF and Forschungszentrum Dresden-Rossendorf FZD. In the appendix, Table 1 gives an overview of the samples supplied and the main deposition parameters. In each deposition charge, 3 fused silica substrates (SQ1, diameter 25 mm, thickness 1 mm, supplied by Gräfe Spezialoptik GmbH, Germany) and 3 silicon substrates have been coated and forwarded to the institutes for analysis. The optical thickness for each layer was required to be $4\lambda/4$ (four times quarterwave thickness) at the wavelength 1064 nm.

2.2. Deposition techniques

As seen from the appendix, the following deposition techniques have been applied:

- Electron beam evaporation without ion assistance (EBE). These layers have been prepared at S1 Optics in a VTD Vera 1400 deposition system as reference samples, in order to obtain strongly shifting layers with low or tensile stress. During deposition, the substrates were heated up to a temperature of 275 °C.
- Electron beam evaporation with ion assistance (IAD) and plasma ion assistance (PIAD). PIAD and IAD samples have been supplied by different participants. PIAD samples have been prepared in Leybold Optics Syrus pro deposition systems (at Fresnel Optics, FISBA OPTIK, IOF, and mso jena). During layer growth, additional energetic ion bombardment has been accomplished by means of the Leybold Advanced Plasma Source APS or APS pro. The IAD samples were produced at Laseroptik Garbsen using BALZERS equipment and an EVATEC (SATIS) ion source. Each partner was free to work with his own favourite deposition parameters in order to prepare samples that show a reasonable compromise between optical and mechanical properties. It was up to the feeling and experience of each participant to define that “compromise” for himself in a reasonable way, there were no predefined target values.
- Magnetron sputtering (MS). A cost-effective reactive pulsed magnetron sputtering of metallic Nb targets has been accomplished at Forschungszentrum Dresden-Rossendorf in a self-developed deposition system [6]. In this case

clear emphasis was made on the development of high-index niobia films with tensile stress and negligible shift. Depositions onto unheated substrates and those heated up to 370 °C were carried out. The substrate normal was either tilted by 17° with respect to the magnetron axis (low plasma flow area) or coinciding with it (high plasma flow area). In the latter case, the film growth rates were up to 2.6 nm/s. Radio-frequency magnetron sputtering of SiO₂ target was used to provide silica films with low thermal shift and mechanical stress.

- Ion beam sputtering (IBS). One SiO₂ sample has been prepared by Laseroptik Garbsen in a VEECO SPECTOR Coater.
- Ion plating (IP). IP samples have been supplied by Evatec Ltd. in an Evatec BAP800 deposition equipment. The samples shall serve as reference for a high-index coating with the lowest possible pore concentration. The layers are expected to show excellent optical properties, but suffering from high compressive stress.

3. Layer characterization

3.1. Film thickness

Ex situ determination of the film thickness has generally been performed in the course of optical characterization as explained in Section 3.2. In addition, selected high refractive index samples have been investigated by cross-sectional transmission electron microscopy TEM, from where we obtained additional information on film thickness and surface roughness of the coatings.

3.2. Optical constants

3.2.1. Variable angle spectroscopic ellipsometry (VASE)

From each deposition charge, the first film on SQ1 has been used for spectroscopic ellipsometry (SE) investigations at FZD. The films were characterized using a VASE spectroscopic ellipsometer (J.A. Woolam Co., Inc., USA), the SE data were acquired and analysed using WVASE software supplied with the ellipsometer (see Refs. [7,8]). The SE data were fitted to a 4-layer model including air, surface roughness, the bulk oxide film, and the fused silica substrate, where the surface roughness was modeled using a 50% air and 50% bulk oxide Bruggeman effective medium [9]. Good fits to the measured Ψ - and Δ -spectra in the 0.75–4.5 eV spectral range were obtained with a normalized mean square error of 1.5–4. An effective thickness of the roughness layer is indicative of the root mean square (rms) value of a short scale surface roughness which does not cause scatter losses [9]. Fused silica optical constants were derived from the SE characterization of the uncoated substrates. The Nb₂O₅ and Ta₂O₅ complex refractive index, $n + ik$, was obtained using a Cody–Lorentz parameterized model [10]. The latter incorporates a weak absorption tail below the band gap and provides significantly better fit to experimental data as Tauc–Lorentz model described in Ref. [11] where this term is absent. In case of HfO₂ and SiO₂ a simple Cauchy parameterization was enough to obtain refractive index of the material. Thus, SE provided film thickness, effective surface roughness, refractive index and extinction coefficient.

The relative error in thickness determination is below 1%, while the relative error in refractive index determination is below 3%.

3.2.2. Spectrophotometry

In parallel to VASE, spectrophotometry at the Perkin Elmer Lambda 900 scanning spectrophotometer has been used to determine the optical constants and thickness of the coatings at Fraunhofer IOF. These measurements have been performed for the second film grown onto a SQ1 substrate from each deposition charge. Transmission (T) and reflection (R) have been measured using a self-developed VN attachment particularly for absolute reflectance measurements. From

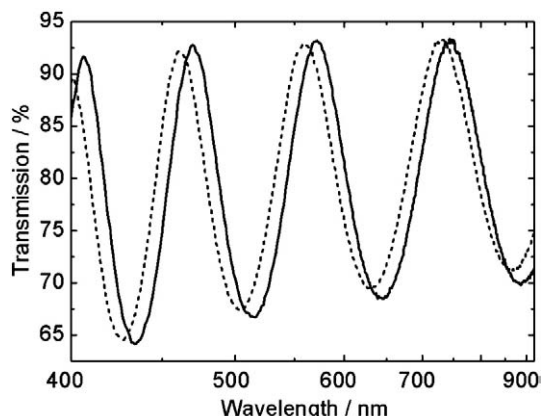


Fig. 1. Transmission of the strongly shifting Nb₂O₅ sample 19 at room temperature (solid) and after heating in vacuum (short dash).

these spectra, film thickness as well as optical constants n (refractive index) and k (extinction coefficient) have been deduced from spectra fits in terms of a Lorentzian multioscillator model [12]. The accuracy in n - and d -determination is of the order of 1% relative error.

3.3. Shift

After conventional T/R -measurements, the thermal shift of the same samples has been determined at IOF from transmission measurements with the OptiMon process spectrophotometer [13]. First, a transmission measurement was performed in atmospheric conditions at room temperature. After that, the measurement chamber has been evacuated to high vacuum and heated up to a temperature of 100 °C before making the second transmission measurement. In both transmission spectra, we made use of an interpolation algorithm to identify the interference maximum at λ_s equal to half the optical thickness of the film, which was located around a wavelength of 550 nm. From the shift of that maximum position, the thermal shift has been calculated by the Equation:

$$\text{shift} = \frac{\lambda_{s,100^\circ\text{C}} - \lambda_{s,\text{room temperature}}}{\lambda_{s,\text{room temperature}}} * 100\% \quad (1)$$

For illustration, Fig. 1 shows normal incidence transmission spectra at room temperature (solid line) and at 100 °C (short dash) obtained from a strongly shifting niobium pentoxide sample. As seen from the envelopes of the interference spectrum, the shift in extrema position is clearly caused by a refractive index decrease due to sample heating. According to Eq. (1), the observed spectral shift corresponds to a thermal shift of -2% . With a specified wavelength accuracy of 0.2 nm and the transmittance measurement accuracy of 0.5%, the wavelength λ_s can be determined with accuracy around 0.5 nm. Therefore the accuracy in shift determination is of the order of 0.1%... 0.2% at least for the high-index samples, where a clear interference pattern appears in the transmission spectrum.

Because the extremum wavelength of the interference pattern is proportional to the optical thickness of the film, Eq. (1) can be rewritten as:

$$\text{shift} = \frac{\Delta(nd)}{nd} * 100\% = \frac{\Delta n}{n} * 100\% + \frac{\Delta d}{d} * 100\% \quad (2)$$

It is thus composed of changes in refractive index itself and a geometrical contribution caused by thermal expansion resulting in an increase of geometrical film thickness d . Although there are no specific values of our film material thermal expansion coefficients available, we estimate the relative increase in the film thickness due to

heating to be around 0.2%, which is consistent to a reasonable thermal expansion coefficient of approximately $2.5 * 10^{-5} \text{ K}^{-1}$. The thermal changes in refractive index can therefore be estimated as:

$$\frac{\Delta n}{n} * 100\% \approx \text{shift} - 0.2\% \quad (3)$$

In practice, the measurement of weak shifts turned out to be impossible for weakly shifting silica samples, due to the low contrast of the interference pattern. In the corresponding graphs the shift was then assumed to be zero.

3.4. Stress measurements

For stress measurements, the curvature of uncoated silicon wafers has been determined at IOF by a Tencor system prior to deposition. After deposition of the film the measurement of the curvature has been repeated, and from the differences in curvature, the layer stress has been calculated by Stoney's Equation [14]. In our convention, negative stress values correspond to tensile, and positive ones to compressive stress. The accuracy in stress determination is strongly dependent on the film thickness. In our case of considerably thick films (film thickness between 450 nm and 800 nm), the absolute error in stress determination is surely below 50 MPa.

3.5. TEM analysis

A number of high-index samples deposited on silicon have been analysed by cross-sectional TEM analysis in order to evaluate the degree and specifics of their porosity as well as of their surface roughness. These measurements have been performed at CM20 instrument (Philips, Netherlands) at 200 kV acceleration voltage. TEM samples were prepared by a standard routine via cutting, gluing, polishing, dimpling and Ar ion milling. Special precautions were made in order to avoid modifications of the amorphous layer structure by the Ar beam during milling.

As a first example, Fig. 2 shows the TEM cross-sectional image of a niobium pentoxide sample obtained from the same deposition run as the sample shown in Fig. 1. This sample has been prepared by pulsed magnetron sputtering prior to any deposition condition optimization. As it turned out to be strongly shifting, we expect a developed network of elongated pores which open at the sample surface. Fig. 2 really confirms the assumed porosity, but in addition, we also get an independent estimation of geometrical film thickness as well as on peak-to-valley roughness at the film surface, which is here about

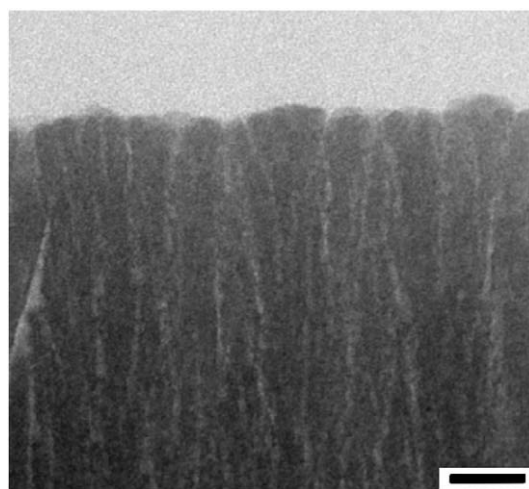


Fig. 2. TEM cross-sectional image of the rather porous niobium pentoxide sample 19. Black bar length 20 nm.

15 nm. Because the characteristic lateral extensions of the roughness profile are surely smaller than the wavelength, we deal with the same type of short scale roughness as in the evaluation of VASE data, so that the peak-to-valley roughness obtained by TEM can be directly compared to the rms-value obtained by VASE analysis. Per definition, the rms-value must of course be significantly smaller than the peak-to-valley roughness, depending on the precise roughness profile.

3.6. Stoichiometry

Stoichiometry of the samples was analysed by elastic recoil detection analysis (ERDA) [15] at FZD. The third sample on silicon from each deposition run was used for that analysis. The experiments were performed by bombarding the sample with 35 MeV Cl^{7+} ions at an angle of 15° relative to the film surface. The scattered ions and the recoils were detected with a Bragg-ionization chamber placed at a scattering angle of 30° . In order to determine hydrogen concentration, the ERDA setup used an additional Si-detector with Al foil in front of it to separate all scattered ions and recoils from hydrogen. A particular task was to compare the hydrogen content in the films with the porosity characteristics obtained from TEM analysis.

4. Results

4.1. Geometrical parameters

All quantitative data on geometrical film parameters are presented in the appendix (Table 2). Table 2 gives an overview on the geometrical parameters obtained by means of different techniques. Regarding geometrical and optical thickness, the ellipsometric and photometric data are in agreement within the mentioned error limits, the deviations between the thicknesses determined by the two methods look purely stochastic without any systematic contributions.

The rms-roughness data obtained from ellipsometry were significantly lower than the peak-to-valley data obtained from TEM, so that the picture here is completely consistent.

For practical purposes it is of interest to note, that

- Layers with crystalline fractions (HfO_2) show a trend to higher surface roughness than amorphous coatings (Nb_2O_5 , Ta_2O_5), which is not astonishing, and;
- Layers deposited by PIAD and IP are in trend smoother than EBE and MS layers.

4.2. Optical and mechanical properties

Although complete dispersion curves have been determined for all samples, we restrict discussion here to the refractive indices n and extinction coefficients k at the wavelength of 400 nm. These data are again listed in the appendix (Table 3) together with results on the determined shift and layer stress. We notice that for each of the high-index materials, a rather broad range of refractive indices could be covered by the deposition techniques applied, so that we can expect to observe and discuss correlations between refractive indices and other (including structural) layer characteristics. Concerning the shift, we cover the range between strong negative shifts of around -2.1% up to positive values of 0.4% . Moreover, we observe a rather diverse stress behaviour starting from tensile stress values around -190 MPa via nearly stress-free samples (of utmost interest for practical applications!) up to high compressive stress values of 540 MPa. Additionally, one of the HfO_2 IP samples exhibits an extremely high stress of 2450 MPa.

EBE samples (low n , strong negative shift, low or tensile stress) and IP samples (high n , weak positive shift, high compressive stress) therefore tend to mark the extreme points in the observed data range, while MS, PIAD and IAD samples fill the range between these

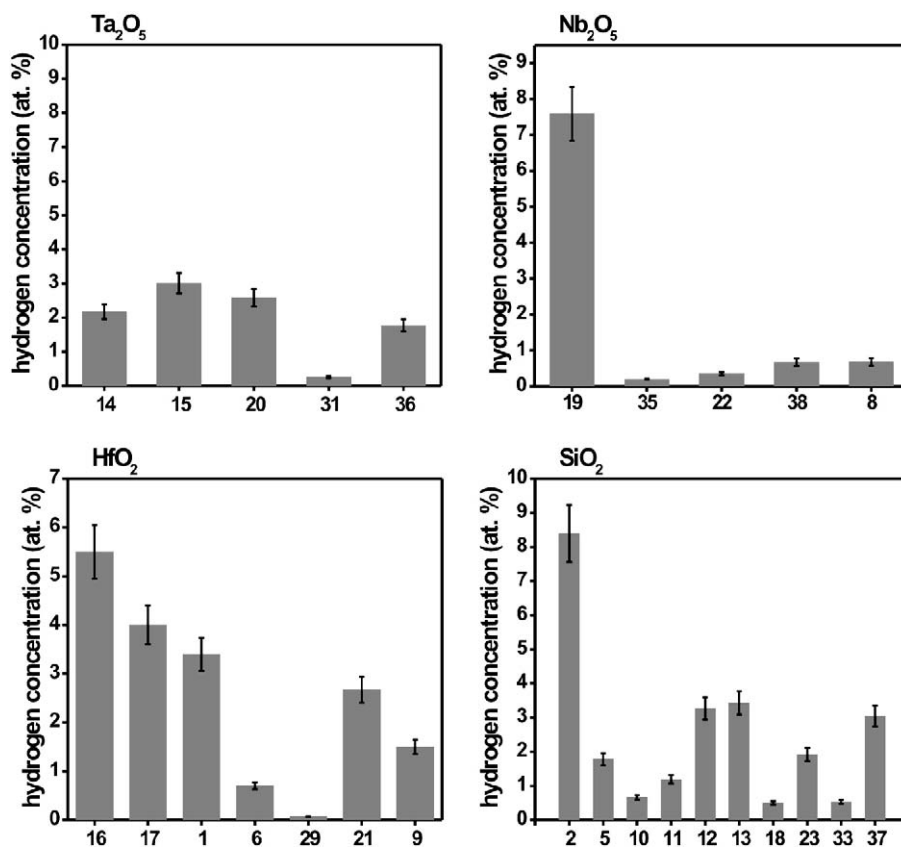


Fig. 3. Hydrogen concentration in the samples according to ERDA measurements. Data are given in at. %.

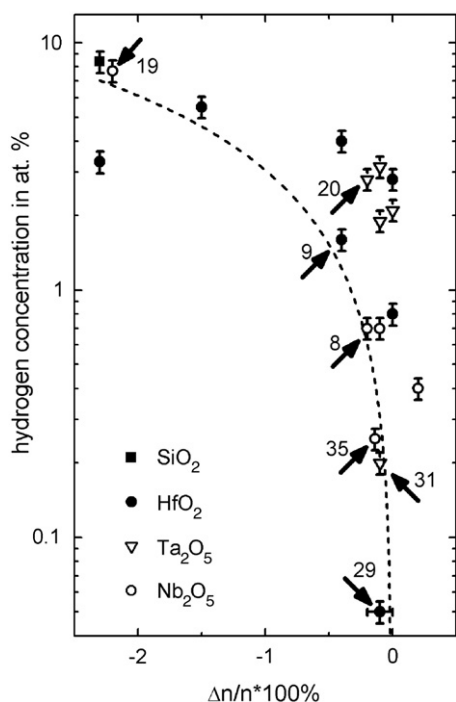


Fig. 4. Thermal shift in refractive index as estimated from measurement data in Table 3 by means of Eq. (3) versus hydrogen concentration data from Fig. 3. The dashed line serves as eye-guideline, it corresponds to a linear fit of the experimental points with forced intersection of the point of origin (note that the scale is logarithmic). Arrows indicate the samples for which TEM images are presented. SiO_2 samples with no detectable shift (see Table 3) are not shown in this graph. For better visibility, horizontal error bars are only shown for sample 29.

extremal points, depending on deposition conditions, more or less continuously.

The optical and mechanical properties of the films were correlated with hydrogen content (ERDA) and partly with the film morphology (cross-sectional TEM).

4.3. Stoichiometry and hydrogen content

Generally, all samples turned out to be nearly ideally stoichiometric. Main differences between the samples can however be identified with respect to their hydrogen content, as shown in Fig. 3.

Experimentally, we obtain a rather strong quantitative correlation between the hydrogen content and the measured shift, as demonstrated in Fig. 4. Therefore, the obtained hydrogen is attributed to atmospheric water, which penetrates into the pores of the coating but tends to leave the coating when the latter is heated, thus causing the measured thermal shift.

4.4. Selected results of TEM investigations

4.4.1. General remarks

In order to obtain a representative picture, the following high-index samples have been investigated by TEM:

- Samples 1 and 19 as representatives for strongly shifting layers with significant tensile stress. Large open pores are expected (and observed, as already demonstrated in Fig. 2).
- Samples 29 and 31 as representatives for the highest index layers with the highest compressive stress. Also sample 22 with moderate compressive stress. No pores (or a few very tiny pores) are expected.
- Samples 8 and 9 as (P)IAD samples with the interesting property combination of zero or small shift, high indices and stronger tensile stress. Also samples 20 and 35 with moderate tensile stress. We

expect pores to be present, but they should occupy only a low volume fraction to explain the high indices. Moreover, they should be closed or very small in diameter, in order to prohibit water penetration (explaining the low shift). At the same time, the tensile stress can then be explained as resulting from the high surface curvature of low-diameter pores.

A few more samples have been investigated in order to verify the results (see Table 2), but they will not be shown explicitly below.

4.4.2. Niobia samples

The niobia samples 8, 19, 22 and 35 have been investigated. All samples turned out to be amorphous.

The pore structure of sample 19 has already been shown in Fig. 2, the obvious abundance of extended open pores explains the strong shift, the tensile stress, the low refractive index and the high hydrogen content (Fig. 3) in this sample.

On the contrary, particularly the high resolution image shown in Fig. 5 shows a completely different type of pores, as obtained for the IAD sample 8. This sample again shows significant tensile stress but is at the same time nearly shift-free and has very low hydrogen content (Fig. 3). Therefore we interpret the picture as an image of *closed nanosized pores* in niobium pentoxide.

Sample 35 is the niobia sample with the highest refractive index, but it still shows (weak) tensile stress. The sample has also been

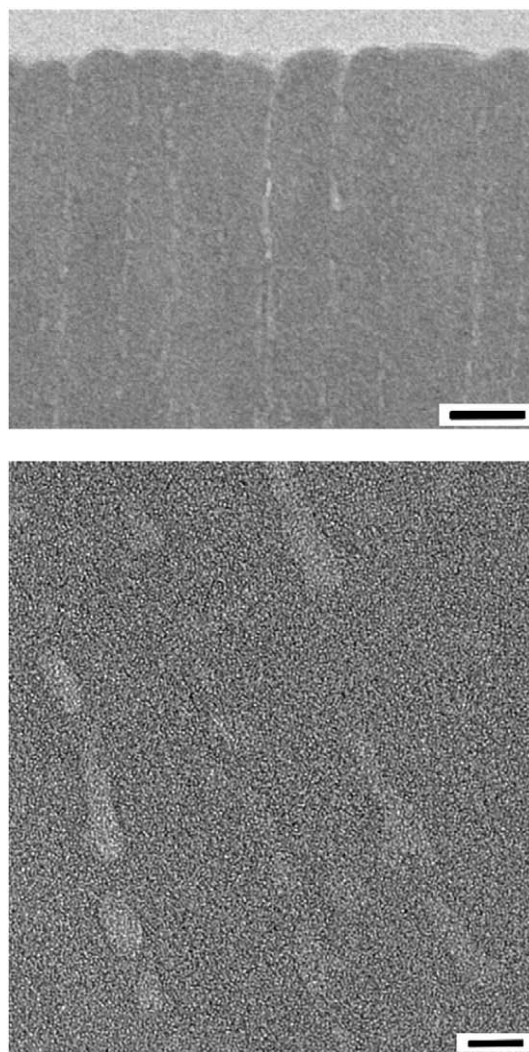


Fig. 5. TEM image of the niobium pentoxide sample 8. Top: overview, black bar length 20 nm; bottom: high resolution image of the pore structure, black bar length 5 nm.

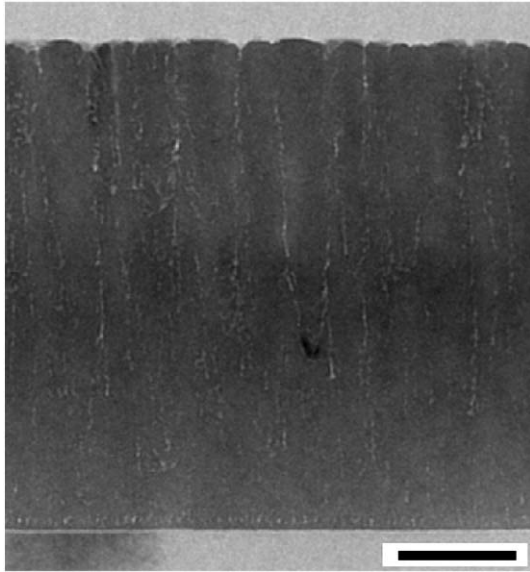


Fig. 6. TEM image of the sputtered niobium pentoxide sample 35. Black bar length 100 nm.

produced by sputtering, but it shows the result of the optimization cycle of sputtering parameters. It was utmostly interesting to correlate its properties to the TEM image, which is shown in Fig. 6. Again, the main fraction of the pores is expected to be closed, in agreement to the low hydrogen content of the sample (Fig. 3). In contrast to all other samples, we find here a chain of localized small pores close to the interface to the substrate (on bottom of the figure). This chain of pores seems to buffer the mechanical stress from the upper region of the film, but it has no remarkable influence on the optical properties because of its small spatial extensions. It also cannot contribute to the shift, because the pores are closed and far from the surface. So that this particular type of spatial distribution of nanoscopic pores in the film allows for a rather extraordinary combination of high average index, low tensile stress and negligible shift.

Sample 22 exhibits significant compressive stress combined with a positive shift and a high refractive index. In a TEM image (not shown here), only a very small number of tiny round pores could be identified, their number was obviously too small for stress relaxation.

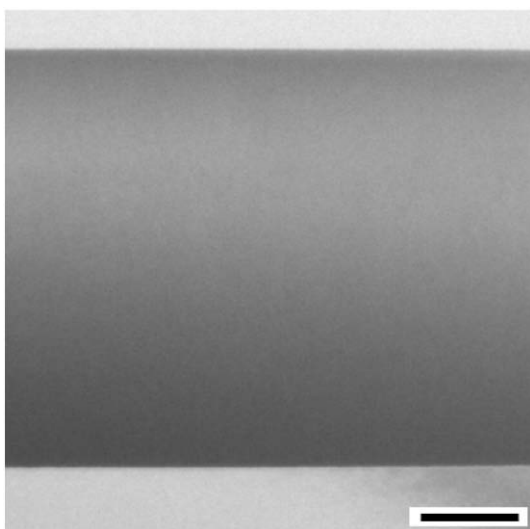


Fig. 7. TEM image of sample 31 (tantalum pentoxide produced by ion plating). Black bar length 100 nm.

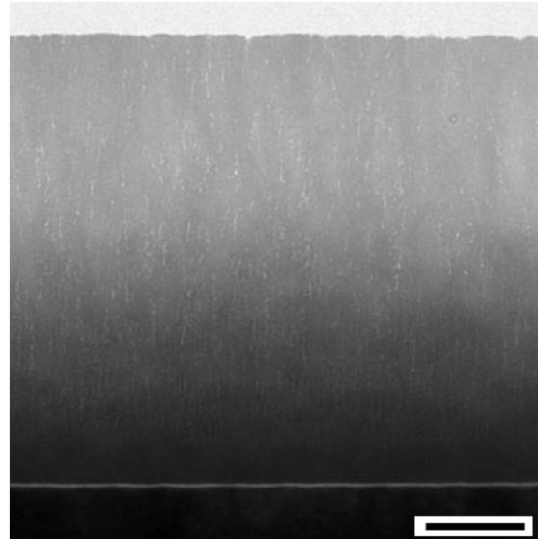


Fig. 8. TEM image of sample 20 (tantalum pentoxide produced by PIAD). Black bar length 100 nm.

4.4.3. Tantalum pentoxide samples

The investigated samples again turned out to be amorphous. We show the images of the IP sample 31 (Fig. 7) and the PIAD sample 20 (Fig. 8). In the TEM image of sample 31, no pores can be identified. The sample has the highest refractive index of all tantalum pentoxide samples, but it also shows the highest compressive stress and a small positive shift. The refractive index of sample 20 (Fig. 8) is lower (but still acceptable), corresponding to a clearly visible pore fraction in the TEM image. The sample is nevertheless shift-free and shows tensile stress. These macroscopic properties as well as the pore structure are qualitatively close to what has been observed for the niobia sample 8.

4.4.4. Hafnia samples

The hafnia samples tend to include significant crystalline fractions, and we demonstrate here the images of two almost crystalline samples. The image of the IP sample 29 (Fig. 9) shows large crystalline grains that are tightly pressed together. Both refractive index and compressive stress of this sample are extraordinarily high, the hydrogen content (Fig. 3) is vanishing. On the contrary, the TEM

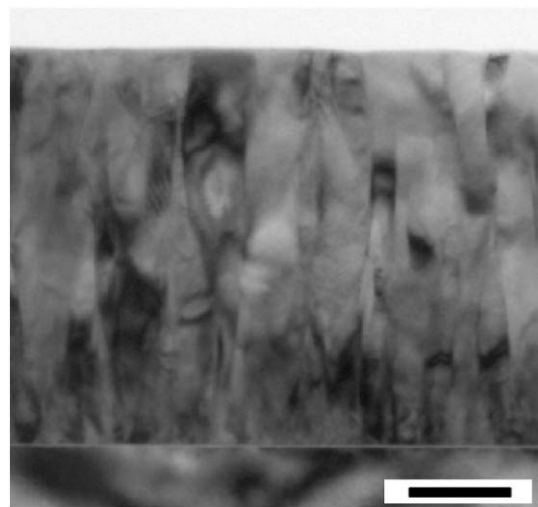


Fig. 9. TEM image of sample 29 (hafnia, deposited by ion plating). Black bar length 100 nm.

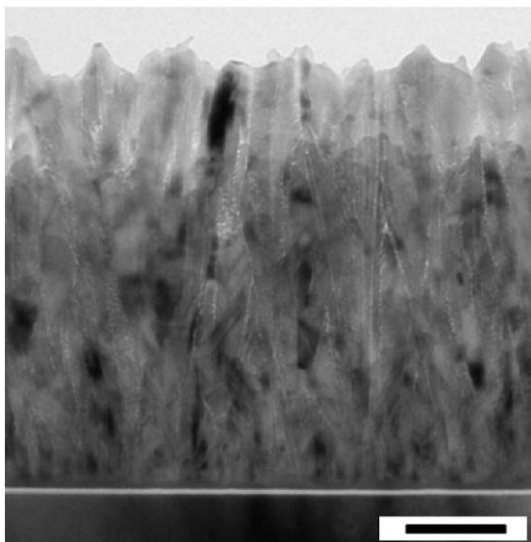


Fig. 10. TEM image of sample 9 (hafnia, deposited by IAD). Black bar length 100 nm.

image of the IAD sample 9 (Fig. 10) shows crystalline grains that are separated from each other by thin elongated pores. This is accompanied by a somewhat lower refractive index and a somewhat higher shift and hydrogen content compared to sample 29, but a tremendous reduction in stress.

Concerning the degree of crystallinity, we only mention that sample 6 turned out to be amorphous, and the remaining PIAD samples contained crystalline as well as amorphous fractions. The usual picture was that the layers started to grow as amorphous layers, later changing to crystalline growth. Therefore, some of the hafnia samples appeared to be slightly inhomogeneous with respect to their optical properties.

5. Discussion

5.1. Property correlations

Fig. 11 shows the measured shift data versus the mechanical stress, all quantitative data taken from the appendix, Table 3. Although the data points stem from four different layer materials, all points arrange more or less closely to a knee-like structure, so that a rather universal behaviour is obtained.

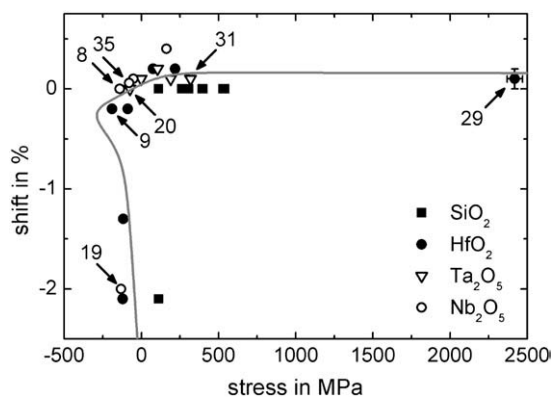


Fig. 11. Shift versus mechanical stress. Symbols correspond to experimental data, the grey line corresponds to the theoretical curve. Arrows indicate the samples for which TEM images are presented. The error bars as shown for sample 29 are representative for all data points.

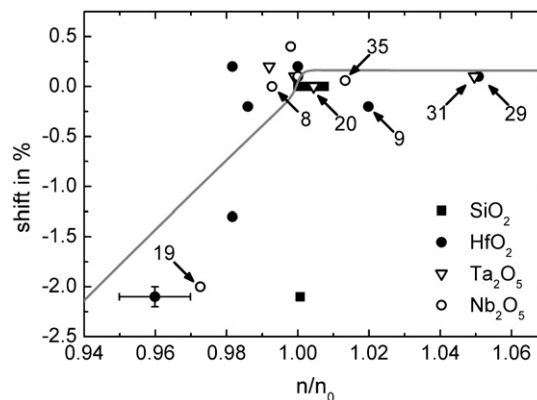


Fig. 12. Shift versus normalized refractive index. Symbols correspond to experimental data, the grey line corresponds to the theoretical curve. Arrows indicate the samples for which TEM images are presented. The error bars as shown for one sample (left on bottom) are representative for all data points.

Of course, it would be useful to check whether or not the relations of shift and stress to the refractive index could be visualised in a similarly universal dependence. In order to do so, we normalized the refractive indices obtained for each material to the refractive index n_0 of the sample with the lowest absolute value of the mechanical stress. All these normalized indices (further denoted as n/n_0) are now close to 1, they are also given in Table 3. Their relation to shift and stress is graphically visualised in Figs. 12 and 13.

In both of these graphs we recognize that the data are again arranged in some knee-like structure. Nevertheless that structure is not as clearly observed as in Fig. 11, particularly it seems that the hafnia data points scatter stronger than the datapoints from the other materials. It is in agreement with varying degree of HfO_2 film crystallinity, while the other materials are almost amorphous as determined by TEM. Particularly, samples 9 and 29 are crystalline, sample 6 turned out to be amorphous, and the remaining samples contain both fractions. Therefore, instead of a two-component mixture (solid fraction and pores), the hafnia samples should in principle be regarded as a three-component mixture (crystalline solid fraction, amorphous solid fraction and pores), which explains the less regular arrangement of the corresponding datapoints. There is another more general problem which concerns the comparison of experimental data obtained from samples deposited on different substrates. Indeed, refractive index data as well as shift data stem from samples deposited on silica, while stress, hydrogen content and TEM are determined from samples deposited on silicon. There are at least

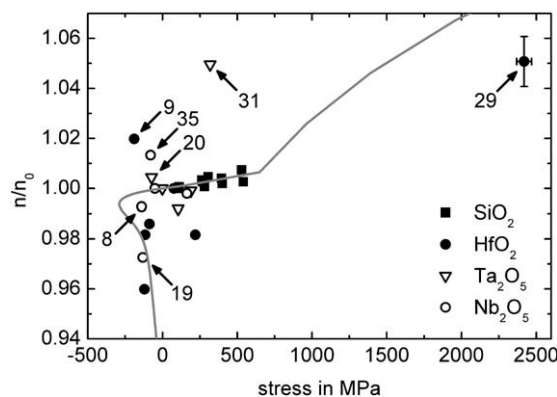


Fig. 13. Normalized refractive index versus mechanical layer stress. Symbols correspond to experimental data, the grey line corresponds to the theoretical curve. Arrows indicate the samples for which TEM images are presented. The error bars as shown for sample 29 are representative for all data points.

three indications that it does nevertheless make sense to compare the data:

- There is generally a native SiO₂-layer on the silicon surface, so that film growth does not start directly on silicon, but rather on SiO₂.
- With the exclusion of sample 29, all samples investigated by TEM were shown to be either amorphous or at least to start growing in an amorphous phase even on a silicon substrate. This is exactly what would be expected for growth on fused silica as well.
- For selected samples, we determined the refractive index from reflection measurements of coatings deposited on the same silicon wafers, which have been used for stress measurements. The obtained indices turned out to be identical to those obtained from samples deposited on SQ1 within the error limits.

It is absolutely clear that all the material characteristics discussed here are complicated functions of a variety of parameters, which may be intrinsic (and specific for a given material) or extrinsic. The observed more or less universal correlation between stress, shift and refractive index suggests that it could be caused by an extrinsic mechanism which is valid for all the coating materials regarded. The further discussion is to show, in how far the different degree of porosity in the samples explains the experimental behaviour of shift, stress and refractive index. We will particularly show that the appearance of the knee-like structures in Figs. 11–13 may be attributed to the presence and specifics of the pores. In that context we demonstrate that considerably simple model assumptions on the porosity effects allow us to reproduce such knee-like structures theoretically.

5.2. Model assumptions and simulation results

In order to verify in how far the observed dependencies are consistent with our assumptions on the role of porosity, a model has been developed that links porosity, refractive index, shift and stress together. The main assumptions of this model are outlined below; the theoretical apparatus behind the calculations is subject of a separate publication [16].

The main (and in fact simple) model assumptions are:

- Pores are regarded to be of cylindrical shape, the pore axis is perpendicular to the film surface.
- The pores are embedded in the solid material, they can either be closed, or they open at the film surface.
- Pores tend to induce tensile stress. Tensile stress becomes stronger with decreasing pore radius.
- The appearance of pores tends to reduce the effective refractive index of the coating in agreement with a Bragg Pippard mixing model [12], however with the pores being regarded as inclusion in a solid host.
- Open pores cause a negative thermal shift.
- Closed pores do not cause any shift.
- An increase in the pores volume fraction in the film is accompanied with an increase in pore radius, as well as an increase in the relative abundance of open pores compared to closed pores.

Concerning the shift, the introduced model allows calculating of the value $\Delta n/n$ (see Eqs. (2) and (3)). In order to compare the theoretical results with the experiment, the full theoretical shift is then calculated via Eq. (3). However, the thermal expansion of the film leads to a decrease in the film density, thus causing a further negative contribution to $\Delta n/n$, which is not directly connected to the pore fraction and therefore not considered in the mentioned model assumptions. Nevertheless in our calculation this effect has been taken into account by a correction term, making use of the Lorentz–Lorenz-Equation [12].

Basing on these assumptions, the grey curves in Figs. 11–13 have been obtained adjusting the free parameters in the model to typical

niobium pentoxide data [16]; the thus obtained curves are obviously consistent with our experimental findings. Let us shortly comment the theoretical curves.

In each of the theoretical curves, the right upper part corresponds to a highly densified medium without any pores, where we expect the experimental points for the IP samples to be located. This part of the curves is characterized by high compressive stress, high refractive index and a small positive shift. The other end of the grey curves corresponds to samples with a high porosity, while the pores are assumed to be large and open. The refractive index is low here, the shift significant and negative, the stress is tensile but small (the stress should be zero in the degenerate case when the layer consists only of pores). The EBE-reference samples might be expected to contribute to the experimental data in this region. Moving in the graphs along the grey lines from the upper right to the lower left end, we consecutively pass the regions of:

- *Weak porosity:* In our graphs pores start to appear approximately at the point where the stress is around +650 MPa. This point may be most easily identified in Fig. 13. As assumed in the simulation, the pores should here be small and closed.
- *First open pores appear:* At this point, the shift starts to decrease from its initial value; it is best identified from the “knee structure” in Fig. 12. In the simulation, it corresponds to an overall porosity of approximately 0.5%.
- *Enough pores for compensating the initially compressive stress:* The coating has low or negligible stress, at the same time the shift is low or zero. The refractive index is still at an acceptable level. This point marks a possibly optimum compromise between the discussed optical and mechanical film parameters. In the simulation, this point corresponds to an overall porosity of approximately 1.1%.
- *Enough (and mostly open but still small in diameter) pores for maximum tensile stress:* The refractive index is already significantly reduced, the shift is negative. This point is identified from the “knee structures” in Figs. 11 and 13. In the simulation, the overall porosity is here approximately 2.4%.
- A further increase in porosity does now relax the tensile stress, while the negative shift becomes stronger, and the refractive index lower. This region is of no practical interest for our purposes.

Particularly from the grey lines in Figs. 11 and 13 it turns out, that shift and refractive index is not necessarily unambiguously related to the film stress. From here we understand, for example, the seemingly strange correlation between the properties of the niobia samples 8 and 19. Both samples show nearly the same tensile stress, but have quite different shift and refractive index values. In the figures these samples simply fall into quite different “porosity” regions.

5.3. Main conclusions

A detailed comparison between theory and experiment confirms that the majority of experimental data points really fall into the correct areas in the graph. For example, samples 35, 8, and 20 are clearly porous; there are moreover strong indications that at least a significant part of these pores is closed. The corresponding data points are consequently located near the “knee structures” of the grey curves. Sample 9 tends to exhibit small but nevertheless predominantly open pores and has therefore a stronger negative shift. The strongly porous samples 1 and 19 are arranged in the left bottom area, while the practically pore-free samples 29 and 31 are more or less reliably found in the right top area of the graphs.

From here we conclude, that the developed model really reflects the main features of the interplay between refractive index, stress, shift and porosity. And both the TEM investigations and the simulations verify that the presence of a certain pore fraction is helpful to obtain a reasonable balance between optical and mechanical layer properties.

Let us for simplicity define the point of optimal property balance as the point at the grey curves where the shift is zero. At this point, the stress is generally small and the refractive index although not at maximum, but still acceptable. In fact, all high-index layers with compressive stress have shown a positive thermal shift, while a vanishing shift was always connected with small or moderate tensile stress (as also predicted by theory). For practical purposes it is important to note, that it is then the comparably easy-to-be-performed shift measurement, which is (at least for high-index layers) relevant for identifying that suggested optimum point. Moreover, in the vicinity of that optimum, both refractive index and stress are unambiguous theoretical functions of the shift (see theoretical curves in Figs. 11 and 12), so that the shift measurement is theoretically capable of controlling the other parameters of interest. This approach is of course only applicable for homogeneous single layers, the parameter optimization for multilayer systems requires more independent measurements.

Finally it must be emphasized, that our experimental data confirm the possibility to produce coatings with balanced properties by means of (P)IAD and MS by suitable choice of the deposition conditions.

6. Summary

In the present study, thin films of practically relevant oxides have been prepared by different deposition techniques and analysed by a variety of characterization techniques. We were able to demonstrate strong correlations between refractive index, thermal shift and mechanical stress of the layers.

Appendix A

The optical constants shown here correspond to the spectrophotometric results. Missing shift data correspond to samples where the shift determination failed (see Section 3.3). “n.d.” means “not detectable”.

A detailed investigation of the hydrogen content and the layer morphology led us to the conclusion, that the main features in the correlation between shift, stress and index are controlled by the specifics of the pore fraction in the films. This conclusion is in agreement with the results of model simulations.

In order to achieve a practically reasonable balance between optical and mechanical properties, a certain pore fraction in the coatings seems to be necessary. The absence of thermal shift in a coating material may be used as experimental criterion that a given film is close to that balance of properties. Several of our high-index oxide layers really show the favourable property combination of high index, vanishing shift and moderate tensile stress. And finally, because all of our low-index (SiO₂)-samples have shown compressive stress, a moderate tensile stress in the high-index materials is prospective in order to partly compensate the SiO₂-induced compressive stress in an optical multilayer stack.

Acknowledgments

S. Wilbrandt, N. Kaiser and O. Stenzel are grateful to H. Haase and G. Kühne (both IOF) for technical support, as well as to S. Jahnke (University of Applied Sciences Jena) and Karen Friedrich (Chemnitz University of Technology) for assistance in manuscript preparation.

M. Vinnichenko, A. Koliutsch and F. Munnik would like to thank B. Schmidt and B. Scheumann (FZD) for assistance with SiO₂ film preparation.

The authors are grateful to the Europäische Forschungsgesellschaft Dünne Schichten e.V. (EFDS) and to the *Arbeitsgemeinschaft industrieller Forschungsvereinigungen “Otto von Guericke”* e.V. (AiF) for financial support.

Table 1
Overview on samples and deposition parameters to the extent as individually disclosed by the companies.

Supplier	No	Material		Method	Specific parameters where applicable and disclosed				
		Film material	Starting material		Deposition system	BIAS voltage for (P)IAD in V or equivalent	Substrate temperature °C	Deposition rate nm/s	O ₂ -flow sccm
S1 Optics	1	HfO ₂		EBE	VTD Vera 1400				
	2	SiO ₂			–				
Fresnel Optics	5	SiO ₂		PIAD	Leybold Syrus pro				
	6	HfO ₂			120 APS pro				
Laseroptik Garbsen	8	Nb ₂ O ₅		IAD	EVATEC (SATIS) ion source				
	9	HfO ₂	Hf		140				
	10	SiO ₂			200				
	11	SiO ₂			200				
mso jena	11	SiO ₂		IBS	VEECO SPECTOR Coater (1250 V)				
	12	SiO ₂			65				
	12	SiO ₂		PIAD	Leybold Syrus pro				
	13				140 APS				
	14	Ta ₂ O ₅		160 APS pro					
	15			125 APS pro					
	16	HfO ₂		120 APS					
FZD	17			120 APS pro					
	18	SiO ₂		MS	Modified Roth&Rau system				
	19	Nb ₂ O ₅	Nb		<100				
	35	Nb ₂ O ₅	Nb		Power 510 W				
35	Nb ₂ O ₅	Nb	Power 625 W						
IOF	20	Ta ₂ O ₅		PIAD	Leybold Syrus pro				
	21	HfO ₂			100 APS pro				
	22	Nb ₂ O ₅	NbO _x		120 APS pro				
	23	SiO ₂			100 APS pro				
Evatec	29	HfO ₂		IP	Evatec BAP800				
	31	Ta ₂ O ₅			0.3				
	33	SiO ₂			0.3				
FISBA OPTIK	36	Ta ₂ O ₅		PIAD	Leybold Syrus pro				
	37	SiO ₂			113 APS				
	37	SiO ₂			180				
	38	Nb ₂ O ₅			180				
	38	Nb ₂ O ₅			100 APS				

Table 2
Roughness, thickness and optical thickness of the layers.

Material	Sample	Roughness in nm		Geometrical thickness <i>d</i> in nm			<i>n</i> at 400 nm		Optical thickness <i>nd</i> at 400 nm	
		Elli (rms)	TEM (peak-to-valley)	Elli	T/R	TEM	Elli	T/R	Elli	T/R
Nb ₂ O ₅	8	3	~5	486	482	480	2.471	2.464	1201	1188
	19	6	~15	499	504	460	2.447	2.414	1221	1217
	22	1	~3	484	481	~480	2.468	2.477	1195	1191
	35	4	~17	457	461	443	2.540	2.515	1161	1159
	38	1		467	464		2.496	2.482	1165	1152
Ta ₂ O ₅	14	3		495	497		2.238	2.221	1108	1104
	15	2		501	501		2.238	2.239	1121	1122
	20	3	~8	511	510	~500	2.248	2.249	1149	1147
	31	1		474	473	~470	2.352	2.350	1115	1112
	36	2		505	504	~485	2.243	2.237	1133	1127
HfO ₂	1	9	~20	553	566	540	2.025	1.986	1120	1124
	6	1		543	548		2.059	2.031	1118	1113
	9	6	~50	521	530	~512	2.124	2.110	1107	1118
	16	6	~30	570	568	560	2.037	2.031	1161	1154
	17	4	~5	536	539	~520	2.048	2.040	1098	1100
	21	4		543	543		2.080	2.069	1129	1123
SiO ₂	29	1		501	508	470	2.197	2.174	1101	1104
	2	n.d.		n.d.	731		n.d.	1.486	n.d.	1086
	5	1		730	732		1.504	1.496	1098	1095
	10	n.d.		n.d.	737		n.d.	1.486	n.d.	1095
	11	1		733	735		1.500	1.489	1100	1094
	12	2		750	744		1.497	1.489	1123	1108
	13	1		736	726		1.498	1.491	1103	1082
	18	n.d.		n.d.	746		n.d.	1.485	n.d.	1108
	23	<1		523	502		1.490	1.492	779	749
	33	1		718	726		1.498	1.488	1076	1080
37	n.d.		n.d.	759		n.d.	1.490	n.d.	1131	

"Elli" denotes ellipsometry results. "n.d." means "not detectable."

Table 3
Optical and mechanical layer properties.

Material	Sample	Deposition technique	<i>d</i> in nm	Mechanical stress in Mpa	<i>n</i> at 400 nm	<i>n</i> / <i>n</i> ₀	<i>k</i> at 400 nm	Shift in %
Nb ₂ O ₅	8	IAD	482	−140	2.464	0.993	0.0003	0
	19	MS	504	−132	2.414	0.973	0.0004	−2.0
	22	PIAD	481	163	2.477	0.998	0.0004	+0.4
	35	MS	461	−80	2.515	1.013	0.0005	+0.06
	38	PIAD	464	−52	2.482	1	0.0006	+0.1
Ta ₂ O ₅	14	PIAD	497	104	2.221	0.992	0.0001	+0.2
	15	PIAD	501	−2	2.239	1	0.0001	+0.1
	20	PIAD	510	−74	2.249	1.004	0.0001	0
	31	IP	473	318	2.350	1.05	0.0003	+0.1
	36	PIAD	504	189	2.237	0.999	0.0001	+0.1
HfO ₂	1	EBE	566	−121	1.986	0.960	0.0006	−2.1
	6	PIAD	548	219	2.031	0.982	0.0004	+0.2
	9	IAD	530	−190	2.110	1.02	0.0005	−0.2
	16	PIAD	568	−117	2.031	0.982	0.0006	−1.3
	17	PIAD	539	−88	2.040	0.986	0.0010	−0.2
	21	PIAD	543	76	2.069	1	0.0004	+0.2
SiO ₂	29	IP	508	2419	2.174	1.051	0.0008	+0.1
	2	EBE	731	111	1.486	1.001	0.0003	−2.1
	5	PIAD	732	529	1.496	1.007	n.d.	−
	10	IAD	737	280	1.486	1.001	n.d.	−
	11	IBS	735	540	1.489	1.003	0.0001	−
	12	PIAD	744	267	1.489	1.003	n.d.	−
	13	PIAD	726	394	1.491	1.004	n.d.	−
	18	MS	746	110	1.485	1	n.d.	−
	23	PIAD	502	305	1.492	1.005	0.0001	−
	33	IP	726	399	1.488	1.002	n.d.	−
37	PIAD	759	262	1.490	1.003	0.0001	−	

The optical constants shown here correspond to the spectrophotometric results. Missing shift data correspond to samples where determination failed (see sect. 3.3.). "n.d." means "not detectable."

References

[1] A. Thelen, Design of Optical Interference Coatings, McGraw-Hill Book Company, New York, 1989.
 [2] N. Kaiser, H.K. Pulker (Eds.), Optical Interference Coatings, Springer-Verlag, Berlin Heidelberg New York, 2003.
 [3] H.A. Macleod, Thin-Film Optical Filters, Adam Hilger Ltd., Bristol, 1986.
 [4] A.V. Tikhonravov, Appl. Opt. 32 (1993) 5417.
 [5] H.K. Pulker, S. Schlichtherle, in: C. Amra, N. Kaiser, H.A. Macleod (Eds.), Proc., 5250, SPIE, 2004, p. 1.
 [6] A.I. Rogozin, M.V. Vinnichenko, A. Kolitsch, W. Möller, J. Vac. Sci. Technol. A. 22 (2004) 349.
 [7] WVASE Software Manual, J.A. Woollam Inc. USA.
 [8] J.A. Woollam, B. Johs, C.M. Herzinger, J. Hilfiker, R. Synowicki, C.L. Bungay, SPIE Critical Reviews of Optical Science and Technology CR72 (1999) 3 WVASE Software Manual, J.A. Woollam Inc. USA.
 [9] D.E. Aspnes, J.B. Theeten, F. Hottier, Phys. Rev. 20 (1979) 3292.

- [10] J. Price, P.Y. Hung, T. Rhoad, B. Foran, A.C. Diebold, *Appl. Phys. Lett.* 85 (2004) 1701.
- [11] G.E. Jellison, F.A. Modine, P. Doshi, A. Rohatgi, *Thin Solid Films* 313/314 (1998) 193.
- [12] O. Stenzel, *The Physics of Thin Film Optical Spectra – An Introduction*, Springer-Verlag, Berlin Heidelberg, 2005.
- [13] S. Wilbrandt, O. Stenzel, N. Kaiser, M.K. Trubetskov, A.V. Tikhonravov, *Appl. Opt.* 47 (2008) C49.
- [14] R. Thielsch, A. Gatto, N. Kaiser, *Appl. Opt.* 41 (2002) 3211.
- [15] U. Kreissig, R. Gago, M. Vinnichenko, P. Fernández-Hidalgo, R.J. Martín-Palma, J.M. Martínez-Duart, *Nucl. Instrum. Methods Phys. Res. B* 219–220 (2004) 908.
- [16] O. Stenzel, *J. Phys. D: Appl. Phys.* 42 (2009) 055312.